Available online at www.sciencedirect.com
ScienceDirect
Trans. Nonferrous Met. Soc. China 34(2024) 1893−1907
Transactions of Nonferrous Metals Society of China
www.tnmsc.cn

Heterogeneous microstructure and mechanical properties of carbon-doped FeCoCrNiMn high-entropy alloy

Lin GUO[1,2], Ji GU[2], Yi-long DAI[1], Jian-guo LIN[1], Min SONG[2]

1. School of Materials Science and Engineering, Xiangtan University, Xiangtan 411105, China
2. State Key Laboratory of Powder Metallurgy, Central South University, Changsha 410083, China

Received 21 December 2022; accepted 3 July 2023

Abstract: Heterogeneous microstructure with nano-precipitate and bimodal grain size distribution was obtained in a FeCoCrNiMn high-entropy alloy (HEA) doped with 0.5 at.% C by a controlled thermo-mechanical treatment. The coarse $M_{23}C_6$ carbides tend to aggregate along the fine grain boundaries. Compared to the sample with homogenous microstructure, the heterostructure FeCoCrNiMn−0.5at.%C HEA has approximately the same average grain size of 4.8 μm. However, it shows bimodal grain size distribution and higher volume fraction of the fine grains (<3 μm), resulting in the increase of yield strength from 552 to 632 MPa. The sample with heterostructure presents different mechanical responses and deformed microstructures in different regions, accounting for significant strain localization and high density of the geometrically necessary dislocations during tensile deformation. These deformation characteristics are beneficial to the enhancement of strain hardening capacity, thereby promoting strength−ductility synergy.

Key words: high-entropy alloy; heterogeneous microstructure; bimodal grain; mechanical properties; strengthening mechanism

1 Introduction

High-entropy alloys (HEAs) have recently acquired much attention due to their promising properties and novel alloy design strategy [1−5]. Among all the HEAs classes, the most studied cases are constructed from five 3d-transition elements (Fe, Co, Cr, Ni, Mn) and have face-centered cubic (FCC) structure [4,6,7]. One representative HEA with FCC structure is the equimolar FeCoCrNiMn alloy, which has high ductility and extremely high toughness at room temperature and even extreme cryogenic temperatures (77 K), but has rather low yield strength at room temperature [6,8,9]. Generally, the HEAs with single FCC structure have a good ductility but a low yield strength due to simple strengthening mechanism, which restricts their demands for engineering applications [4]. In view of the dilemma in strength and ductility, a scientific and technological challenge is to increase the strength of FCC structured HEAs without significantly sacrificing the ductility.

Encouragingly, a novel strategy aimed at producing heterogeneous microstructure with a bimodal grain size distribution has been developed to overcome the strength−ductility trade off [10−15]. The bimodal grains contain a mixture of coarse grains and ultrafine grains. The coarse grains contribute to the strain hardening and ensure large retained ductility, while the ultrafine grains are responsible for the increase of the strength [16].

Corresponding author: Jian-guo LIN, Tel: +86-15080788918, E-mail: lin_j_g@xtu.edu.cn;
Min SONG, Tel: +86-731-88877677, E-mail: msong@csu.edu.cn
DOI: 10.1016/S1003-6326(24)66514-3

Moreover, the bimodal grains endow the alloy with extra work hardening capacity, which is attributed to the storage of geometrically necessary dislocations from a large plastic gradient during deformation [17]. However, it has only a few successful examples in obtaining heterogeneous grain size distribution in bulk materials, such as via severe plastic deformation at cryogenic temperature [10], asymmetric rolling followed by secondary recrystallization [13], or powder metallurgy route [14,15]. For example, the powder metallurgy route to prepare bimodal grains has a complex two-step process: the first step is creating an ultrafine-grained shell by applying severe plastic deformation to micro-sized powders via mechanical milling or high-energy ball milling, and the second step is consolidating powders by spark plasma sintering or hot roll sintering [14,15].

Generally, the nanoprecipitates are believed to restrict the grain growth during recrystallization, leading to the formation of an ultrafine-grained structure [18]. Hence, the introduction of nano-precipitates has potential to prepare bimodal grains in bulk materials. Furthermore, the achievement of high strength requires multiple strengthening mechanisms, such as the grain refinement, the precipitation hardening and the interstitial-solid solution strengthening [19−21]. As a result, the alloy compositions and thermo-mechanical treatment should be carefully considered to obtain proper heterogeneous microstructure and thus achieve excellent mechanical properties. The addition of interstitial elements, i.e., carbon [20,22] and nitrogen [23,24], is one of the most effective ways to increase the strength of HEAs based on 3d transition elements. For example, the high strength of carbon-doped HEAs benefits from both interstitial-solid solution strengthening and precipitation hardening due to the dissolved carbon atoms and the formation of carbides during annealing process [20,22,25]. According to the previous investigations, the $M_{23}C_6$ carbides can effectively inhibit the FCC grain growth in the carbon-doped HEAs [20].

In the present study, the equimolar FeCoCrNiMn HEA doped with 0.5 at.% C was selected as the target material. Conventional cold rolling and annealing treatment were used to prepare the heterogeneous microstructure with precipitates and bimodal grain size distribution. The alloy was firstly cold-rolled and subsequently annealed at 650 °C to form heterogeneous micro-structure involving nonuniformly distributed carbides and non-fully recrystallized structure. Then, the sample was annealed at 750 °C to obtain a fully recrystallized structure but with heterogeneous distribution of grain size and precipitates. The detailed microstructural characterization and two-dimensional hardness map research were conducted to investigate the heterogeneous microstructure and the local mechanical properties. The microstructural evolution was systematically analyzed to understand the deformation mechanisms.

2 Experimental

The equimolar FeCoCrNiMn HEA with 0.5 at.% C was prepared from pure metals and graphite powder by arc-melting method under Ar atmosphere. Pure titanium was melted before melting to absorb residual oxygen in the furnace. For the purpose of compositional homogeneity, the graphite powder was placed in the middle layer of the raw materials, and moreover, the ingots were remelted at least four times and flipped over after each melting. The content of the carbon in the alloy was measured to be 0.47 at.% using Leco analyzer. The alloy was hot-rolled at 900 °C to 50% reduction in thickness after homogenization treatment at 1100 °C for 12 h, and was subsequently annealed at 1200 °C for 1 h followed by water-quenching. Then, the homogenized alloy was cold-rolled to 70% reduction in thickness. Three heat treatment processes were used to obtain different micro-structures in the alloy with partial recrystallization, bimodal grain and homogeneous microstructures, defined as PR, BG and HM, respectively. The PR sample was annealed at 650 °C for 2 h followed by water-quenching. The BG sample was annealed at 650 °C for 2 h and then annealed at 750 °C for 0.5 h followed by water-quenching. The HM sample was annealed at 800 °C for 1 h followed by water-quenching.

XRD measurement was performed on the three samples using a Dmax 2500VB X-ray equipment with Cu K_α radiation. The grain size distribution was characterized by the electron backscatter diffraction (EBSD) method, which was conducted on a scanning electron microscope (SEM, FEI Helios NanoLab G3 UC) equipped with TSL OIM

TSL software. Further microstructural characterization, such as the high-resolution TEM (HRTEM) and high-angle annular dark-field (HAADF) techniques, were conducted on an FEI Titan G2 60−300 TEM with a spherical aberration corrector operating at 300 kV. The detail sample preparation processes for EBSD and TEM observation were shown in our previous investigation [17].

Dog-bone-shaped specimens with a gauge length of 24 mm were cut from the alloy sheets for tensile tests. Uniaxial tensile tests were performed on an Instron 3369 testing machine with a strain rate of $1.4\times10^{-3}\ s^{-1}$ at room temperature. Prior to tensile tests, the surfaces of the tensile samples were ground from 400 to 2000 grit using SiC paper.

3 Results

3.1 TEM results of cold-rolled and partial recrystallized samples

Figure 1 shows the TEM images of the cold-rolled alloy. The bright field (BF) image and corresponding selected area electron diffraction (SAED) pattern in Fig. 1(a) demonstrate the presence of nanotwins in this alloy after cold rolling. Figure 1(b) displays the dark field (DF) image of the red rectangle region in Fig. 1(a). And the average thickness of the nanotwins was measured to be 3.2 nm. The dislocation cells were also observed in the alloy, as shown in Fig. 1(c). Meanwhile, some microbands were observed, as shown in Fig. 1(d), which were identified by the SAED insert in Fig. 1(d). The stacking fault energy (SFE) of the FeCoCrNiMn HEA increases by the addition of carbon, which restricts the formation of nanotwins and in turn favors the formation of dislocation cells and microbands [26]. Therefore, all these microstructural features can be observed in the cold-rolled alloy. It should also be noted that carbides or other precipitates were not found in the cold-rolled sample.

Figure 2 displays the TEM image of partial recrystallized (PR) sample. The BF image in Fig. 2(a) shows the non-fully recrystallized and recrystallized regions, indicating the formation of PR microstructure. According to the high-resolution TEM (HRTEM) image and corresponding fast Fourier transformation (FFT) pattern in Figs. 2(b)

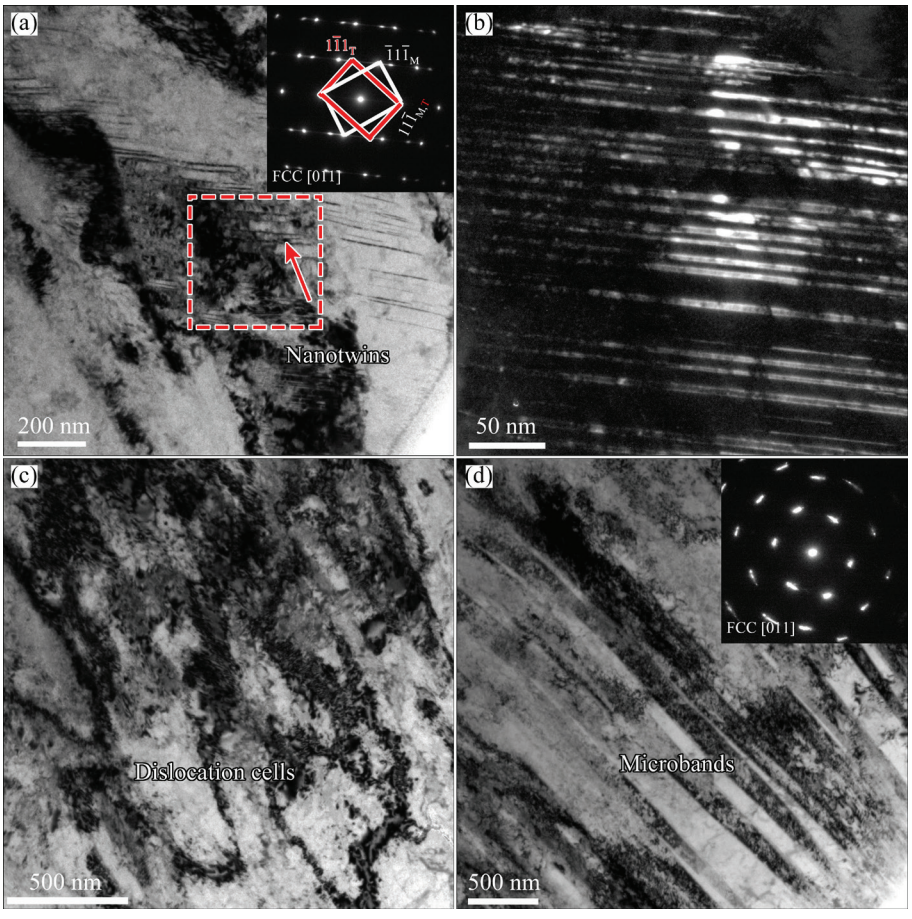

Fig. 1 TEM images of cold-rolled sample: (a, b) Nanotwins; (c) Dislocation cells; (d) Microbands

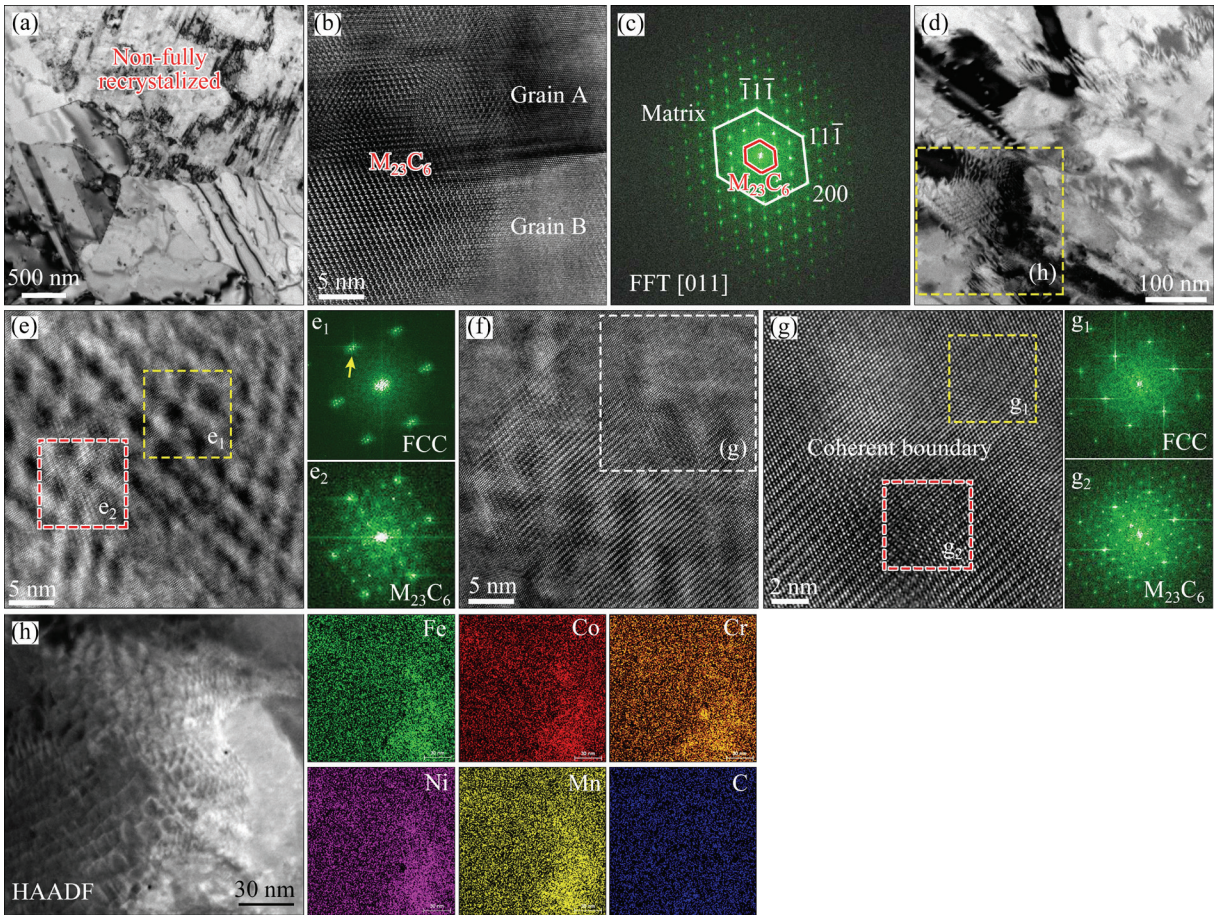

Fig. 2 TEM images of partial recrystallization sample: (a) TEM image showing non-fully recrystallized structure; (b, c) HRTEM and FFT images of grain boundary precipitate, respectively; (d) BF TEM image of incompletely recrystallized region; (e, e_1, e_2) HRTEM and corresponding FFT images of incompletely recrystallized area, respectively; (f) HRTEM image of precipitate in incompletely recrystallized area; (g, g_1, g_2) Enlarged image in (f) and corresponding FFT images, respectively; (h) HAADF image and corresponding elemental distribution maps

and (c), a $M_{23}C_6$ carbide locates along a grain boundary. Figure 2(d) shows the BF image of non-fully recrystallized region and Fig. 2(e) shows the HRTEM image within the non-fully recrystallized region. The corresponding FFT pattern (Fig. 2(e_1)) of the yellow rectangle region in Fig. 2(e) shows satellite reflections around the FCC lattice spots, as denoted by yellow arrow, indicating the presence of elemental clusters [27]. A nano $M_{23}C_6$ carbide with the size of 5 nm can be observed in this elemental cluster region, illustrated by the corresponding FFT pattern (Fig. 2(e_2)) of the red rectangle region in Fig. 2(e). The HRTEM in Fig. 2(f) shows another larger $M_{23}C_6$ carbide with the size of about 25 nm. Based on the magnified image in Fig. 2(g) and corresponding FFT patterns in Figs. 2(g_1) and (g_2), it can be deduced that the $M_{23}C_6$ carbide and the matrix present a fully coherent interface. Figure 2(h) shows the HAADF scanning TEM (STEM) image of the yellow rectangle in Fig. 2(d), which demonstrates the obvious contrast difference in this region. The corresponding elemental mapping clearly illustrates the existence of the elemental clusters.

3.2 Characteristics of heterogeneous structure

Figure 3 shows the back-scattered electron (BSE) images of the PR, HM and BG samples. Figure 3(a) clearly shows the formation of PR structure, and the fraction of non-fully recrystallized regions is measured to be 51.3%. Figure 3(b) demonstrates that the HM sample forms a fully recrystallized structure. The BG sample also has fully recrystallized structure, but the grain size presents a heterogeneous distribution, as shown in Fig. 3(c). Some fine grains prefer to cluster together, indicating the formation of bimodal grain-sized structure. A magnified BSE image shown in

Fig. 3(d) demonstrates that the coarse $M_{23}C_6$ carbides tend to precipitate along the boundaries of the fine grains. Figure 4 displays XRD patterns of the PR, BG and HM samples, indicating the present HEAs with FCC structured matrix. The enlarged image in the 2θ range of 41°−46° is shown in Fig. 4(b). The weak diffraction peak corresponding to the (511) planes of $M_{23}C_6$ carbide is detected in HM sample, but absent in the BG and PR samples. The weakness and absence of $M_{23}C_6$ carbide peaks in the XRD pattern are owing to the low volume fraction of $M_{23}C_6$ carbide, which is identified by LI [28].

The grain size distribution of the BG and HM samples was further analyzed by EBSD technique and the results are shown in Fig. 5. Figures 5(a) and (d) illustrate the inverse pole figure (IPF) maps of the BG and HM samples, respectively. Figures 5(b) and (e) show the distribution of the fine grains with sizes ranging from 0.2 to 3 μm in the BG and HM samples, respectively. These fine grains were denoted by red color. Small regions in the middle of both figures are magnified and shown on the insets for clearer observations. As can be seen, the fine grains in BG sample tend to locally aggregate with each other and form clusters (pointed by the yellow arrows). Instead, the fine grains in HM sample are isolated with each other. In conclusion, the grains present more heterogeneous distribution in BG sample than in HM sample. The fractions of these

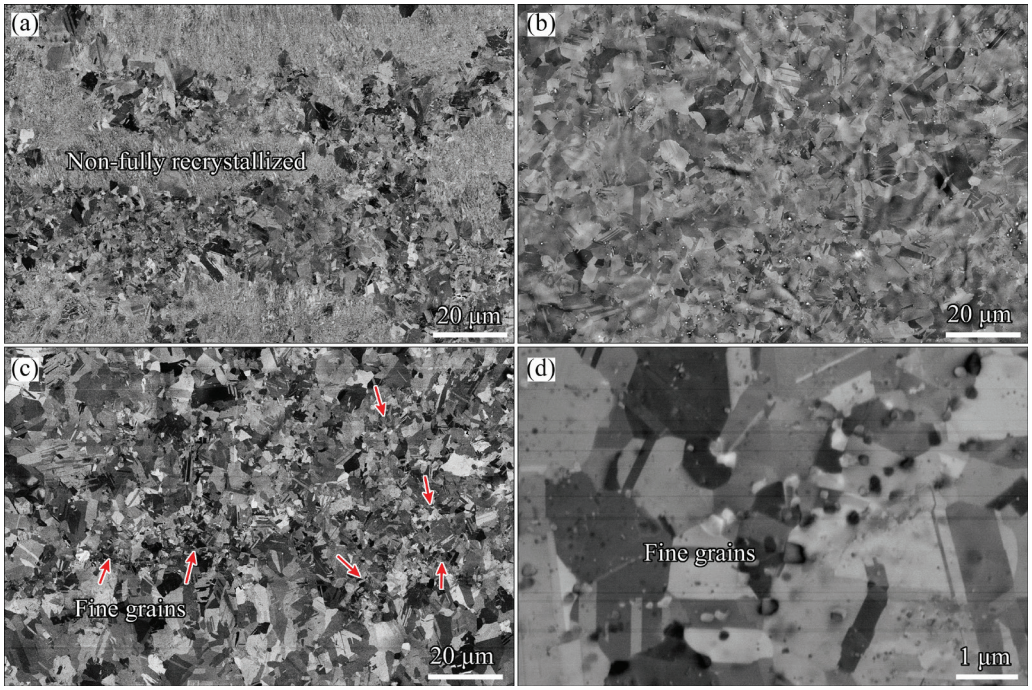

Fig. 3 Backscattered electron images of PR (a), HM (b) and BG (c, d) samples

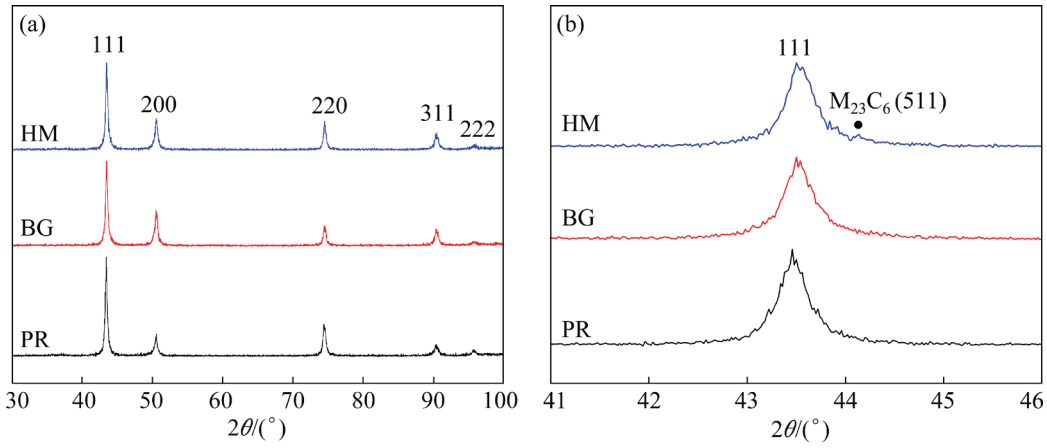

Fig. 4 XRD patterns of PR, BG and HM samples (a), and enlarged patterns in 2θ range from 41° to 46° (b)

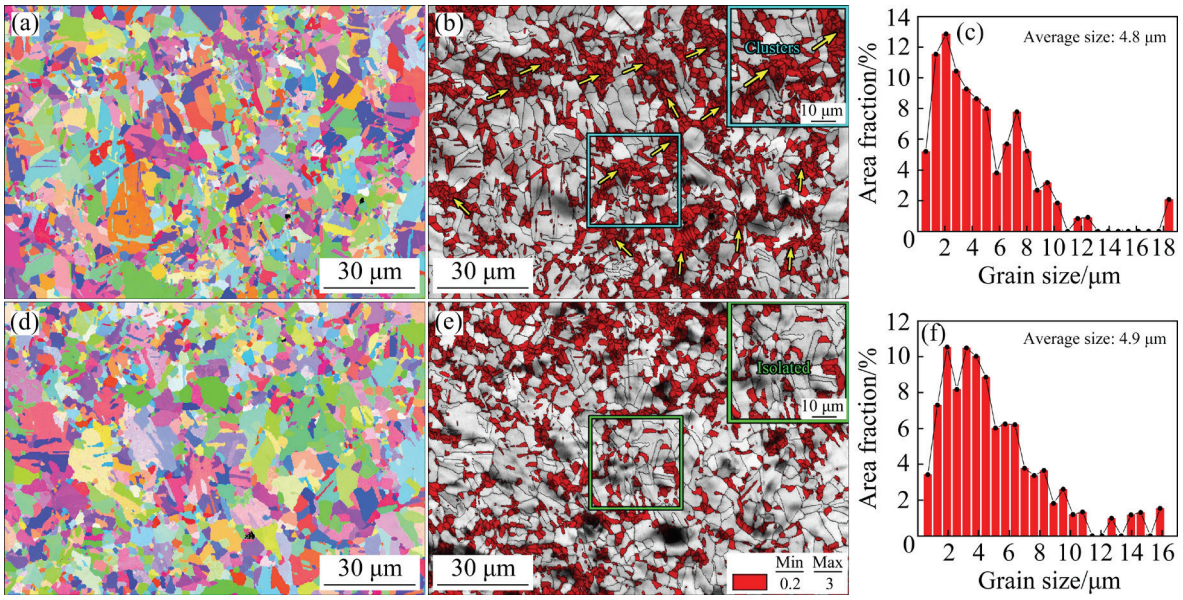

Fig. 5 EBSD IPF maps (a, d), distribution of fine grains (in red) with size ranging from 0.2 to 3 μm (b, e) and statistical distribution of grain size of alloys with two thermomechanical treatments (c, f): (a, b, c) BG sample; (d, e, f) HM sample

fine grains in the BG and HM samples were calculated to be 37.1% and 30.7%, respectively. The statistical distribution of the grain size for both the BG and HM samples is shown in Figs. 5(c) and (f), respectively. The BG sample shows a bimodal grain size distribution, and the average grain sizes of the BG and HM samples were measured to be 4.8 and 4.9 μm, respectively.

The size of the $M_{23}C_6$ particle was statistically measured through the HAADF-STEM image. The HAADF-STEM images of the BG and HM samples are shown in Figs. 6(a) and (c), respectively. Some $M_{23}C_6$ carbides were precipitated in both the BG and HM samples. Figures 6(b) and (d) display the particle size distribution of the BG and HM samples, and the average sizes were measured to be 56.1 and 65.6 nm, respectively. The volume fractions of $M_{23}C_6$ carbides were calculated as 3.6% and 4.3%, respectively. It should be noted that the annealing temperature for the HM sample is higher than that for the BG sample. Since the diffusion rate of elements increases with the increase of the temperature, the high annealing temperature is beneficial to the formation and coarsening of the precipitates. Hence, the $M_{23}C_6$ carbides in the HM sample have a larger size and a higher volume fraction than those in the BG sample.

3.3 Mechanical properties

Figures 7(a) and (b) show the two-dimensional hardness maps of the BG and HM samples using a load of 200 g for 15 s, respectively. The maps present heterogeneous distribution in hardness, especially for the BG samples (Fig. 7(a)). The BG sample has the maximum hardness of HV 307.9 and the minimum hardness of HV 229.2, while the HM sample has the maximum hardness HV 284.6 and the minimum hardness HV 228.6. The standard deviations of the hardness in the BG and HM samples were calculated as HV 18.5 and HV 11.7, respectively. These statistical data further demonstrate the heterogeneous mechanical properties of the BG sample. The heterogeneous microstructure involves $M_{23}C_6$ carbides and bimodal grains in the BG sample, resulting in the variation of the local microstructures, which in turn affects the local mechanical properties.

The typical engineering stress−strain curves for the BG and HM samples are shown in Fig. 8(a). Compared to the HM sample, the yield strength (YS) of the BG sample increases by 14.5% from 552 to 632 MPa, and the ultimate tensile strength (UTS) increases by 7.6% from 830 to 893 MPa with a slight decrease in the ductility from 40% to 36%. Figure 8(b) displays true stress−strain curves for the BG and HM samples. The strain hardening rates derived from the true stress−strain curves are

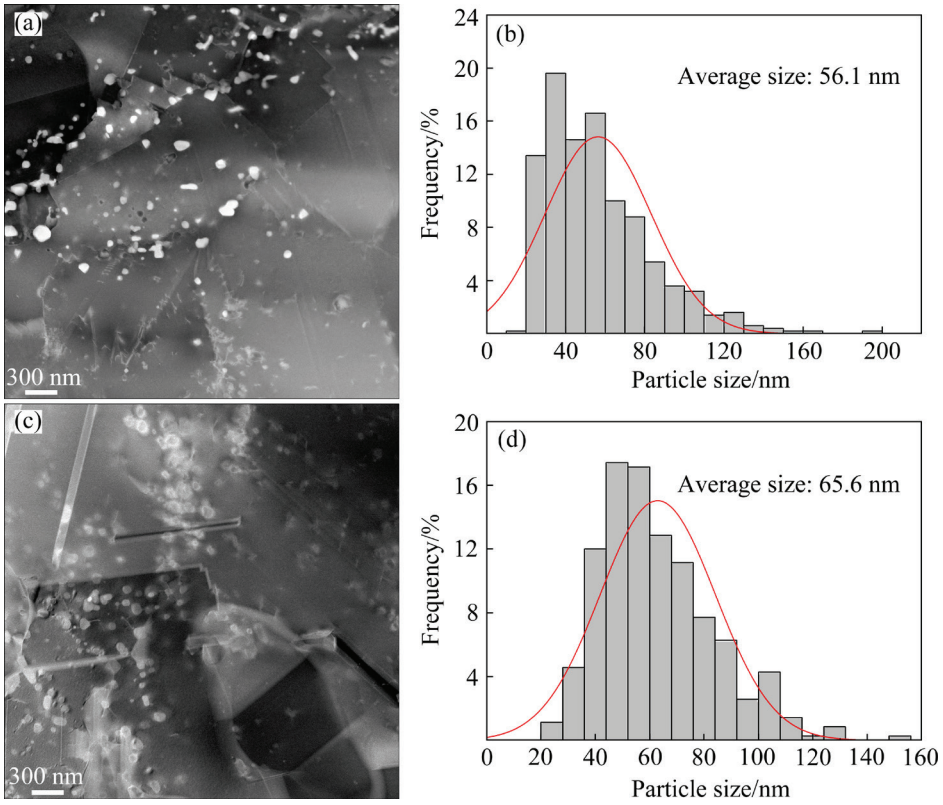

Fig. 6 HAADF-STEM images of BG (a) and HM (c) samples, and $M_{23}C_6$ particle size distribution of BG (b) and HM (d) samples

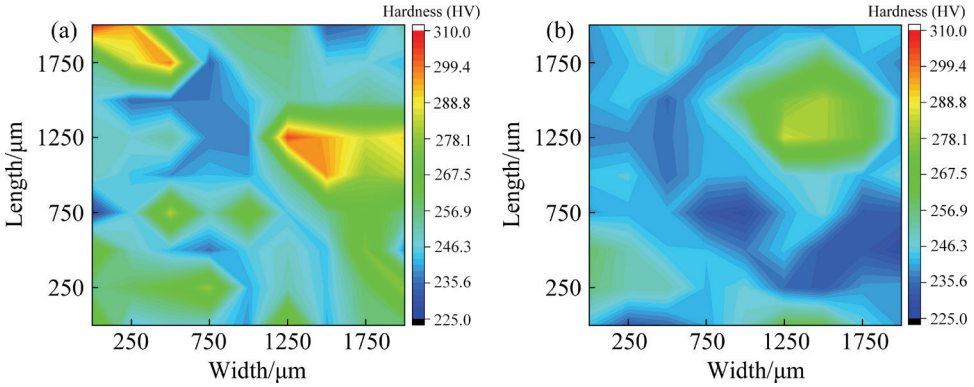

Fig. 7 Two-dimensional hardness maps of BG (a) and HM (b) samples

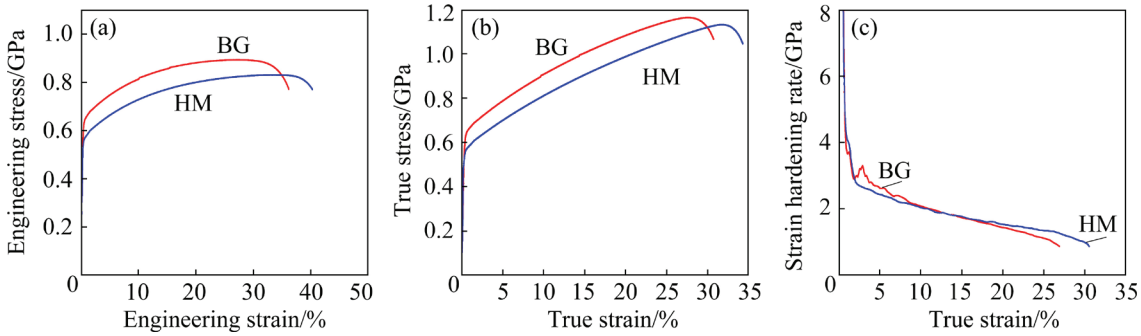

Fig. 8 Tensile properties of FeCoCrNiMn−0.5at.%C HEA after different thermomechanical treatments: (a) Typical engineering stress−strain curves; (b) True stress−strain curves; (c) Strain hardening rate curves

shown in Fig. 8(c). The BG sample has a higher strain hardening rate at the early stage of the tensile deformation with a true strain below 12.5%.

3.4 Deformed microstructures

The deformed microstructures at an engineering strain of 5% for the BG and HM samples were analyzed by EBSD technique, including kernel average misorientation (KAM), grains boundary and geometrically necessary dislocations (GNDs) maps, and the results are shown in Fig. 9. Figures 9(a) and (e) show the IPF maps of the BG and HM samples, respectively. Figures 9(b) and (f) show the KAM maps of the BG and HM samples, respectively, and the statistical distributions are shown in Figs. 9(b_1) and (f_1), respectively. The average values of the KAM for the BG and HM samples were calculated to be 1.08° and 0.79°, respectively. The grain boundary maps of the BG and HM samples are shown in Figs. 9(c) and (g), respectively. The low angle boundaries (LABs, $2°<\theta<15°$) are denoted as red lines, while the high angle boundaries (HABs, $\theta>15°$) are denoted as blue lines. More LABs can be observed in the coarse grains, as shown in Fig. 9(c). The fractions of the LABs for the BG and HM samples were calculated to be 42.6% and 23.6%, respectively. The GNDs maps and statistical distributions for the

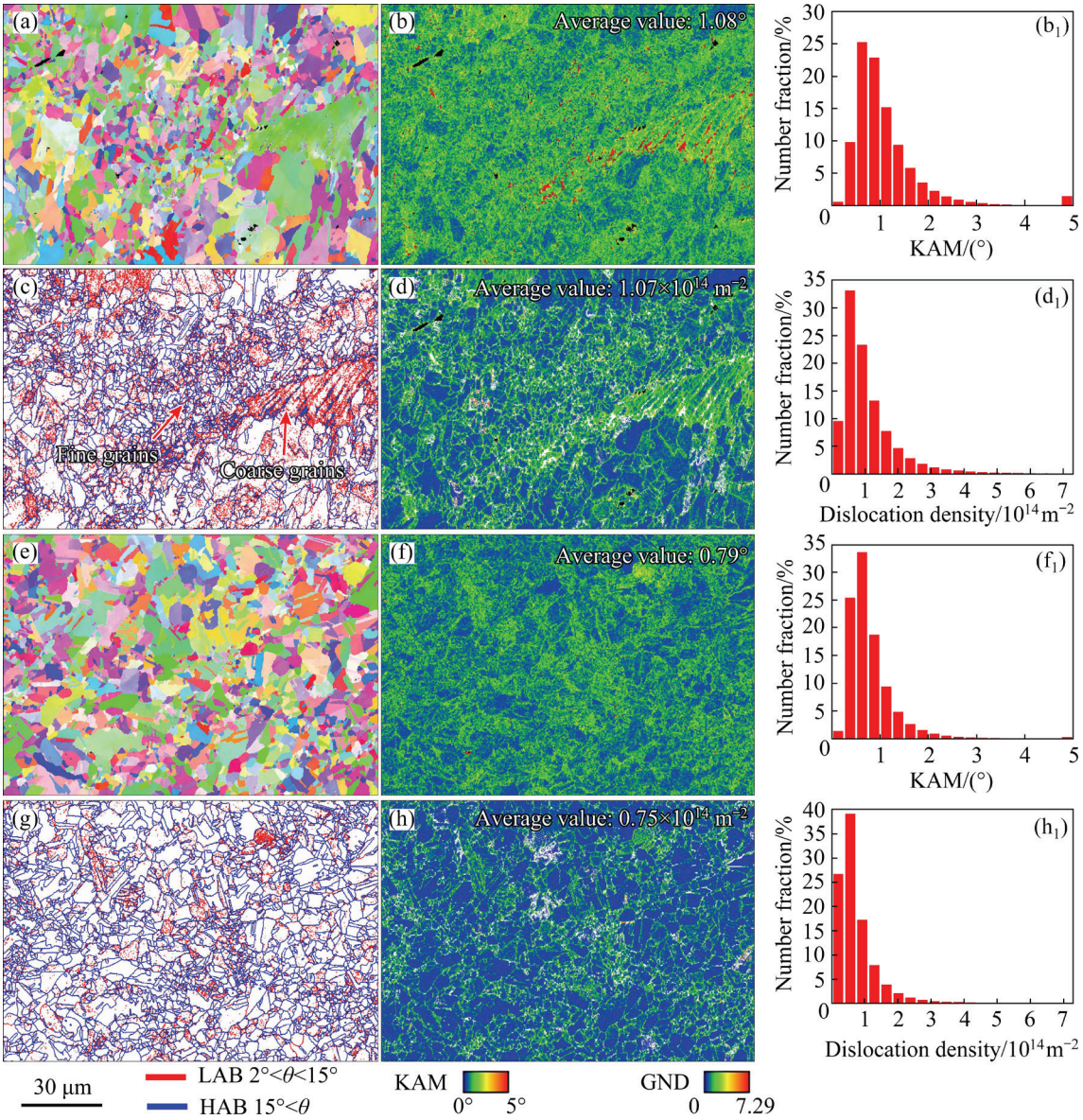

Fig. 9 Deformed microstructure at engineering strain of 5% analyzed by EBSD technique, including IPF (a, e), KAM (b, f, b_1, f_1), grain boundary misorientation (c, g) and geometrically necessary dislocation maps (d, d_1, h, h_1) for BG (a, b, b_1, c, d, d_1) and HM (e, f, f_1, g, h, h_1) samples

BG and HM samples are shown in Figs. 9(d, d_1) and Figs. 9(h, h_1), respectively. The BG sample has a higher average value (1.07×10^{14} m^{-2}) of GNDs than the HM sample (0.75×10^{14} m^{-2}). The grain boundaries tend to have a higher density of GNDs than grains interior.

Interestingly, a coarse grain in the BG sample presents a larger density of GNDs as shown in Fig. 9(d), whose deformed microstructure was further analyzed by combined EBSD and electron backscatter channel contrast image (ECCI) techniques, and the results are shown in Fig. 10. Figure 10(a) shows the IPF map of the coarse grain regions in the BG sample. Some bands that present slight difference in orientations with the matrix are observed inside the coarse grain. Misorientations along the blue and red arrows in Fig. 10(a) are displayed in Fig. 10(b). The misorientation in the coarse grain (red line) is obviously larger than that in the fine grain (blue line). The interfaces between bands and the matrix inside the coarse grain have large misorientations ranging from 6.8° to 14.6°, while the misorientation along the blue line in the fine grain changes only from 0.1° to 1.7°. In Fig. 10(c), more dislocations and microbands can be observed inside the coarse grain while only a few dislocations can be distinguished in the fine grains, indicating that the coarse grains withstand a larger strain than the fine grains at the initial deformation stage. Based on these results shown in Figs. 9 and 10, the heterogeneous deformation and strain localization happened in the BG sample.

The microstructures for the BG and HM samples deformed to fracture were characterized by TEM, and the results are shown in Figs. 11 and 12, respectively. The dislocation tangles, dislocation cells and pile-ups around the $M_{23}C_6$ carbides were observed in the BG samples, as shown in the TEM image in Fig. 11(a). Figure 11(b) shows another TEM image, and a magnified image of the yellow rectangle region in Fig. 11(b) is shown in Fig. 11(c). The corresponding SAED pattern in Fig. 11(c_1) illustrates that a few nanotwins were formed in the BG sample. The TEM image in Fig. 11(d) demonstrates the deformed microstructures around the $M_{23}C_6$ carbides. Figure 11(e) shows the magnified image of the white rectangle region in Fig. 11(d). A few nanotwins were also observed and identified by the corresponding SAED pattern in Fig. 11(e_1). Moreover, the SAED pattern shows that the FCC main diffraction spots present a slight rotation, indicating the severe deformation in this region. The $M_{23}C_6$ carbides impede the slip of dislocations, which produces large stress concentration during deformation, and therefore results in the formation of large orientation gradient around the $M_{23}C_6$ carbides [29]. Hence, the heterogeneous deformation was observed in the BG sample. The TEM images in Figs. 12(a, b) demonstrate that the dislocations pile up around the $M_{23}C_6$ carbide in the HM sample. The TEM images in Figs. 12(c, d) and corresponding SAED pattern in Fig. 12(d_1) also demonstrate the formation of nanotwins in the HM sample after deformation to fracture. The HM sample seems to have more nanotwins than the BG sample.

4 Discussion

4.1 Formation of heterogeneous microstructure

As mentioned above, a heterostructure composed of nano-sized $M_{23}C_6$ carbides and bimodal grains was successfully fabricated in the BG sample by proper thermo-mechanical treatment. The constituent elements diffuse via grain boundary and short-range lattice diffusion, which controls the growth and coarsening of $M_{23}C_6$ carbides [30−32]. Grain boundary and dislocations are crystal defects,

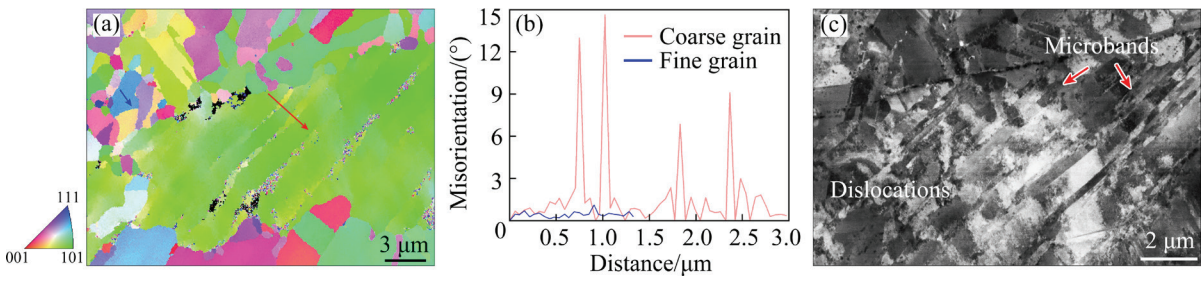

Fig. 10 EBSD IPF map of coarse grain regions in BG sample (a), misorientation (b) along blue and red vectors in (a) and electron backscatter channel contrast image (c)

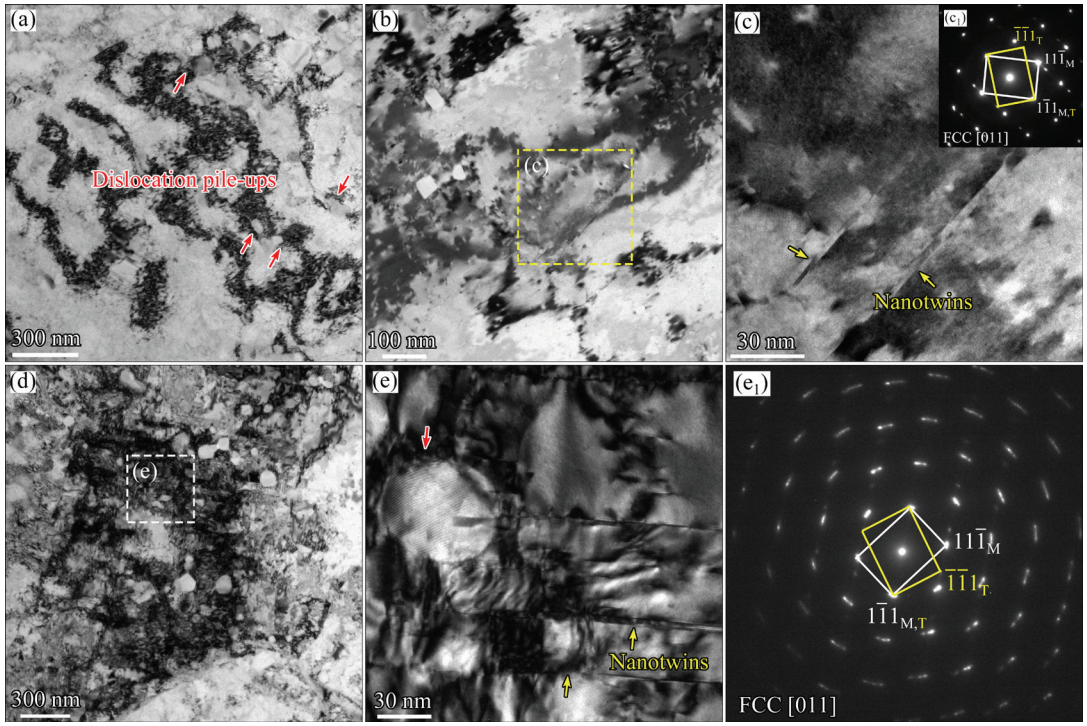

Fig. 11 TEM images of BG sample deformed to fracture: (a) Dislocation pile-ups around $M_{23}C_6$ carbides; (b, c) Few nanotwins and corresponding SAED pattern; (d, e, e_1) Deformed microstructures and corresponding SAED pattern around region with $M_{23}C_6$ carbides

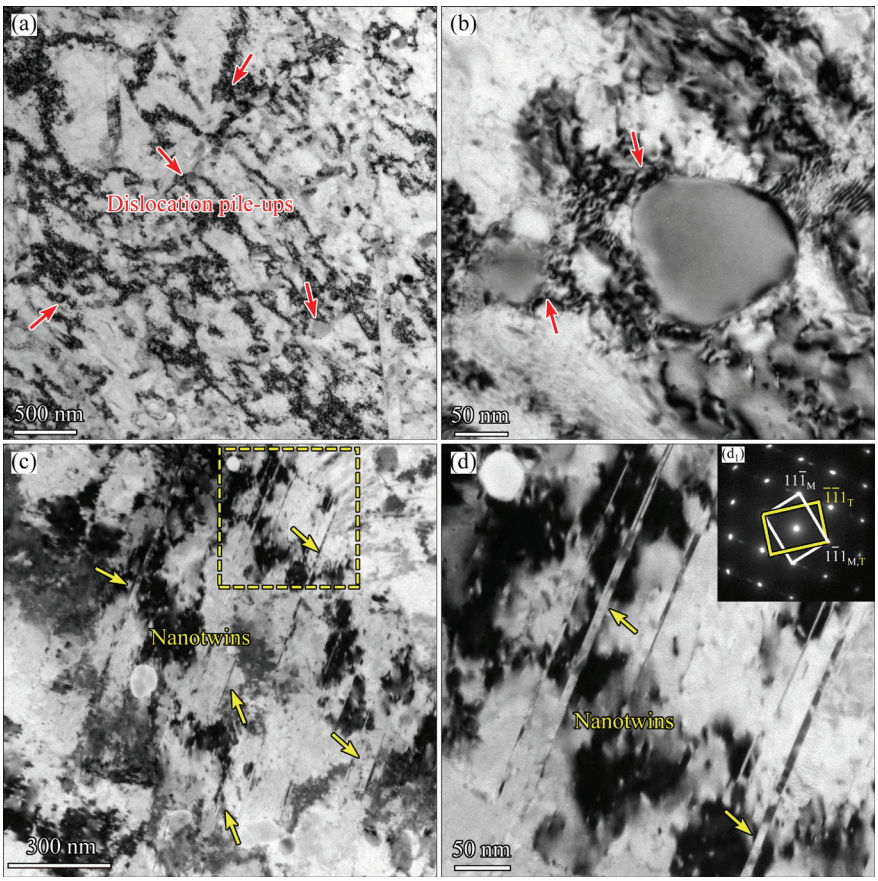

Fig. 12 TEM images of HM sample deformed to fracture: (a, b) Dislocation pile-ups around $M_{23}C_6$ carbides; (c, d, d_1) Few nanotwins and corresponding SAED pattern

which provide a fast channel for diffusion of alloying elements [31]. Hence, the $M_{23}C_6$ carbides were observed both at grain boundaries and inside the grains. The local elemental fluctuation favors the formation of precipitates, resulting in the formation of nanosized $M_{23}C_6$ carbides (~5 nm) within the elemental clusters region.

The cold rolling process introduces a large number of defects, which increases the driving force for the nucleation and coarsening of the precipitates during the subsequently annealing treatment. Hence, the heterogeneously deformed microstructure can lead to inhomogeneous energy required for the nucleation of precipitates. As shown in Fig. 1, the heterogeneously deformed microstructures including nanotwins, dislocation cells and microbands, were observed in the FeCoCrNiMn−0.5at.%C HEA after cold rolling process. As a result, the $M_{23}C_6$ carbides heterogeneously precipitate in the present HEAs via proper thermo-mechanical treatment. In our work, an incompletely recrystallized structure and heterogeneous distribution of the $M_{23}C_6$ carbides were firstly obtained by annealing the alloy at 650 °C for 2 h. Then, the sample was annealed at a higher temperature of 750 °C, which further accelerated the recrystallization behavior and thus a fully recrystallized structure was obtained. As previously studied, the $M_{23}C_6$ carbides can act as barriers for the migration of grain boundaries during annealing [17]. Therefore, its heterogeneous distribution will further aggravate the heterogeneous distribution of the grain size during short-time annealing at a higher temperature of 750 °C, resulting in the formation of bimodal grain size distribution.

4.2 Mechanical properties

The deformation behavior of the BG sample with heterostructure is different from that of the HM sample. Since the mechanical properties between fine grains and coarse grains present incompatibility, and the larger $M_{23}C_6$ carbides at the fine grain boundaries hinder the transfer of strain, the BG sample produces an obvious strain gradient (strain localization) during the tensile deformation. As illustrated by the misorientations of the EBSD images and the high magnification ECCI analysis (Fig. 10), the coarse grains generated larger strains than fine grains. Furthermore, the high density of GNDs was produced to accommodate the strain gradient in the BG sample [33,34]. The density of GNDs (ρ_{GND}) mainly depends on the mechanical properties and the local misorientation angle θ, which can be described by the following expression [33]:

$$\rho_{GND}=\frac{2\theta}{n\lambda b} \tag{1}$$

where b is the amplitude of Burgers vector, λ is the scan step size, and n denotes the average number of nearest neighbors used in the EBSD analysis. In the current experiment, the step size was 0.1 μm and n is the default value of data analysis in the OIM software. Due to the presence of strain gradient, which further enlarges the local misorientation angle θ, the BG sample has higher density of GNDs (1.07×10^{14} m^{-2}) than the HM sample (0.75×10^{14} m^{-2}) at an engineering strain of 5%. The high density of GNDs is beneficial to enhancing strain hardening rate [17]. Therefore, in the early stage of deformation (with a true strain below 12.5%), the BG sample has a higher strain hardening rate. The interaction between nanotwins and dislocation during tensile deformation could improve the capacity of storing dislocations and thus sustain the strain hardening rate [35,36]. Since the volume fraction of $M_{23}C_6$ carbides in the HM sample (4.3%) is higher than that in the BG sample (3.6%), the content of interstitial carbon atoms in the HM sample is lower than that in the BG sample. The carbon increases the stacking fault energy (SFE) of Fe−Cr−Ni-based stainless steels and TWIP steels [37−39]. Due to the similarity of composition and mechanical behavior of the FeCoCrNiMn alloy and austenitic steels, the addition of carbon increases the SFE for FeCoCrNiMn HEA [22]. Thus, the HM sample has lower SFE than the BG sample, leading to the higher twinning activity in the HM sample. The formation of nanotwins increases the capacity of storing dislocations and provides additional strain hardening [2,40,41]. Consequently, the HM sample displays a higher strain hardening rate at the later stage of tensile deformation with a true strain higher than 12.5%.

Table 1 displays the mechanical properties of carbon-contained FeCoCrNiMn HEAs from the current work and also the previous literature. By comparison, the BG sample in this study presents better mechanical properties than previous work.

Table 1 Mechanical properties of carbon-containing FeCoCrNiMn HEAs from current preparation process and previous literature

HEA	Yield strength/MPa	Ultimate tensile strength/MPa	Elongation/%	Source
FeCoCrNiMn−0.5at.%C (BG)	632	893	36	Present work
FeCoCrNiMn−0.5at.%C (HM)	552	830	40	Present work
FeCoCrNiMn−0.5at.%C	225	655	38	[42]
CoCrFeNiMn−1at.%C	570	880	30	[26]
CoCrFeNiMn−1at.%C	634	843	38	[43]
$Co_1Cr_{0.25}Fe_1Mn_1Ni_1$−0.5at.%C	565	851	28	[44]
$Co_1Cr_{0.25}Fe_1Mn_1Ni_1$−2.0at.%C	562	895	32	[44]
FeCoCrNiMn−1.3at.%C	600	836	24	[45]

Obvious strain gradient was observed in the BG sample. On the one hand, the accommodation of this strain gradient needs to produce GNDs, which generates high back stress and makes the softer matrix strong and thus improve the yield strength [13,46]. One the other hand, the plastic deformation of metals is connected with two types of dislocations, statistically stored dislocations and GNDs. The flow stress as a function of dislocation density can be denoted as [47,48]

$$\tau=\alpha Gb\sqrt{\rho_s+\rho_G} \quad (2)$$

where τ is the shear flow stress, α is a constant, G represents the shear modulus, and ρ_s and ρ_G are the densities of statistically stored dislocations and GNDs, respectively. Based on this function, statistically stored dislocations and GNDs have similar contributions to the flow stress. The higher density of the GNDs in the BG sample due to the formation of heterogeneous deformation and strain gradient during tensile deformation leads to the enhancement of the flow stress. Moreover, the nano-carbides exert strengthening effect by Orowan strengthening mechanism, which can be calculated by the Ashby−Orowan equation [49]:

$$\Delta\sigma_{Orowan}=(0.538Gbf^{0.5}/D)\ln[D/(2b)] \quad (3)$$

where G(=68.8 GPa) is the shear modulus adopted from FeCoCrNiMn HEA [50,51], $b=a_0/\sqrt{2}$, with a_0 as the lattice constant of the HEAs, f is the volume fraction of precipitate, and D is the real spatial diameter of precipitate ($D=(3/2)^{0.5}D_0$, where D_0 is the average diameter of the precipitates measured from the intersection plane). The lattice parameter of the present HEAs is 0.361 nm, which is measured from the interplanar distance of {111} planes in the HRTEM image. The detailed measurement method is shown in Fig. S1 in Supporting Materials. Hence, the precipitation strengthening of carbides in BG and HM samples are calculated to be 127.4 and 123.3 MPa, respectively. The lattice friction stress increases ~160 MPa with doped 1 at.% C in FeCoCrNiMn HEA [26], which is attributed to the interstitial solid solution strengthening from the carbon atoms. Unfortunately, it is difficult to accurately measure the difference value in interstitial carbon content between HM and BG samples. However, based on the twinning activities and volume fraction of $M_{23}C_6$ carbides, it seems reasonable to deduce that the content of interstitial carbon atoms in the HM sample is lower than that in the BG sample leading to the lower value of interstitial solid solution strengthening.

Consequently, due to these comprehensive factors, although the BG and HM samples have approximately the same average grains size, the BG sample achieves better combination of strength and ductility than the HM sample. Based on this strategy in designing heterogeneous microstructure and optimizing the synergy of strength and ductility, the topic of our further work will focus on enhancing strain gradient by tailoring SEF to control the deformation mechanisms in fine grains and large grains, and further takes advantage of precipitation strengthening effect by introducing proper precipitates, such as *B*2 and Cu-rich intermetallics.

5 Conclusions

(1) Different deformed microstructures, involving

nanotwins, dislocation cells and microbands were observed in the FeCoCrNiMn−0.5at.%C HEA after cold rolling. The $M_{23}C_6$ carbides precipitate during annealing treatment and present heterogeneous distribution that the coarse $M_{23}C_6$ carbides aggregate along the fine grains boundaries.

(2) The HM (4.9 μm) and BG (4.8 μm) samples present an approximately similar average grain size, but different grain size distribution, which were realized by controlling the thermo-mechanical treatment. The BG sample shows obvious bimodal grain size distribution and high fraction of the fine grains with the size ranging from 0.2 to 3 μm.

(3) Comparing to the HM sample, the deformed microstructure in BG sample presents heterogeneous characteristics, and thus forms strain gradient and produces a higher density of GNDs during tensile deformation. These deformation characteristics favor the enhancement of strain hardening rate and thus improve the yield strength with little loss in the ductility.

CRediT authorship contribution statement

Lin GUO: Investigation, Data curation, Formal analysis, Writing − Original draft, Writing − Review & editing; **Ji GU:** Methodology, Data curation, Formal analysis; **Yi-long DAI:** Formal analysis; **Jian-guo LIN:** Conceptualization, Formal analysis, Writing − Review & editing; **Min SONG:** Conceptualization, Supervision, Formal analysis, Writing − Review & editing.

Declaration of competing interest

The authors declare that they have no known competing financial interests or personal relationships that could have appeared to influence the work reported in this paper.

Acknowledgments

This work was supported by the National Key Research and Development Program of China (No. 2022YFE0134400), the National Natural Science Foundation of China (Nos. 51971247, 51971190), and the Natural Science Foundation of Hunan Province, China (No. 2022JJ30712).

Supplementary Materials

Supplementary Materials in this paper can be found at: http://tnmsc.csu.edu.cn/download/13-p1893-2022-1439-Supplementary_Materials.pdf.

References

[1] MIRACLE D B, SENKOV O N. A critical review of high entropy alloys and related concepts [J]. Acta Materialia, 2017, 122: 448−511.

[2] GEORGE E P, RAABE D, RITCHIE R O. High-entropy alloys [J]. Nature Reviews Materials, 2019, 4(8): 515−534.

[3] GAO M C, YEH J W, LIAW P K, ZHANG Y. High-entropy alloys — Fundamentals and applications [M]. Heidelberg: Springer, 2016.

[4] LI Ze-zhou, ZHAO Shi-teng, RITCHIE R O, MEYERS M A. Mechanical properties of high-entropy alloys with emphasis on face-centered cubic alloys [J]. Progress in Materials Science, 2019, 102: 296−345.

[5] TIAN Yu-sheng, ZHOU Wen-zhe, TAN Qing-biao, WU Ming-xu, QIAO Shen, ZHU Guo-liang, DONG An-ping, SHU Da, SUN Bao-de. A review of refractory high-entropy alloys [J]. Transactions of Nonferrous Metals Society of China, 2022, 32(11): 3487−3515.

[6] CANTOR B. Multicomponent high-entropy cantor alloys [J]. Progress in Materials Science, 2021, 120: 100754.

[7] DU Hui, CAI Jia-hong, WANG Ya-song, YAO Jun-qing, CHEN Qiang, CUI Yu, LIU Xin-wang. Effect of partial recrystallization on microstructure and tensile properties of NiFeCoCrMn high-entropy alloy [J]. Transactions of Nonferrous Metals Society of China, 2022, 32(3): 947−956.

[8] OTTO F, DLOUHÝ A, SOMSEN C, BEI H, EGGELER G, GEORGE E P. The influences of temperature and microstructure on the tensile properties of a CoCrFeMnNi high-entropy alloy [J]. Acta Materialia, 2013, 61(15): 5743−5755.

[9] GLUDOVATZ B, HOHENWARTER A, CATOOR D, CHANG E H, GEORGE E P, RITCHIE R O. A fracture-resistant high-entropy alloy for cryogenic applications [J]. Science, 2014, 345(6201): 1153−1158.

[10] WANG Yin-min, CHEN Ming-wei, ZHOU Feng-hua, MA En. High tensile ductility in a nanostructured metal [J]. Nature, 2002, 419: 912−915.

[11] FU Z Q, MACDONALD B E, LI Z M, JIANG Z F, CHEN W P, ZHOU Y Z, LAVERNIA E J. Engineering heterostructured grains to enhance strength in a single-phase high-entropy alloy with maintained ductility [J]. Materials Research Letters, 2018, 6(11): 634−640.

[12] LI Y, LU Y F, LI W, KHEDR M, LIU H B, JIN X J. Hierarchical microstructure design of a bimodal grained twinning-induced plasticity steel with excellent cryogenic mechanical properties [J]. Acta Materialia, 2018, 158: 79−94.

[13] WU X L, YANG M X, YUAN F P, WU G L, WEI Y J, HUANG X X, ZHU Y T. Heterogeneous lamella structure unites ultrafine-grain strength with coarse-grain ductility [J]. Proceedings of the National Academy of Sciences of the United States of America, 2015, 112(47): 14501−14505.

[14] SAWANGRAT C, KATO S, ORLOV D, AMEYAMA K. Harmonic-structured copper: Performance and proof of fabrication concept based on severe plastic deformation of powders [J]. Journal of Materials Science, 2014, 49(19):

6579−6585.

[15] SEKIGUCHI T, ONO K, FUJIWARA H, AMEYAMA K. New microstructure design for commercially pure titanium with outstanding mechanical properties by mechanical milling and hot roll sintering [J]. Materials Transactions, 2010, 51(1): 39−45.

[16] ZHU Lin-li, SHI San-qiang, LU Ke, LU Jian. A statistical model for predicting the mechanical properties of nanostructured metals with bimodal grain size distribution [J]. Acta Materialia, 2012, 60(16): 5762−5772.

[17] MA E, ZHU T. Towards strength–ductility synergy through the design of heterogeneous nanostructures in metals [J]. Materials Today, 2017, 20(6): 323−331.

[18] CHANG K, FENG W M, CHEN L Q. Effect of second-phase particle morphology on grain growth kinetics [J]. Acta Materialia, 2009, 57(17): 5229−5236.

[19] MECKING H, KOCKS U F. Kinetics of flow and strain-hardening [J]. Acta Metallurgica, 1981, 29(11): 1865−1875.

[20] GUO Lin, OU Xiao-qin, NI Song, LIU Yong, SONG Min. Effects of carbon on the microstructures and mechanical properties of FeCoCrNiMn high entropy alloys [J]. Materials Science and Engineering A, 2019, 746: 356−362.

[21] ZHAO Y L, YANG T, TONG Y, WANG J, LUAN J H, JIAO Z B, CHEN D, YANG Y, HU A, LIU C T, KAI J J. Heterogeneous precipitation behavior and stacking-fault-mediated deformation in a CoCrNi-based medium-entropy alloy [J]. Acta Materialia, 2017, 138: 72−82.

[22] WANG Zhang-wei, BAKER I, GUO Wei, POPLAWSKY J D. The effect of carbon on the microstructures, mechanical properties, and deformation mechanisms of thermo-mechanically treated $Fe_{40.4}Ni_{11.3}Mn_{34.8}Al_{7.5}Cr_6$ high entropy alloys [J]. Acta Materialia, 2017, 126: 346−360.

[23] SONG Min, ZHOU Rui, GU Ji, WANG Zhang-wei, NI Song, LIU Yong. Nitrogen induced heterogeneous structures overcome strength-ductility trade-off in an additively manufactured high-entropy alloy [J]. Applied Materials Today, 2020, 18: 100498.

[24] SON S J, LEE J W, ASGHARI-RAD P, GU G H, HAFTLANG F, KIM H S. A facile strengthening method by co-doping boron and nitrogen in CoCrFeMnNi high-entropy alloy [J]. Materials Science and Engineering A, 2022, 846: 143307.

[25] PENG Jian, LI Zi-yong, JI Xin-bo, SUN Yan-le, FU Li-ming, SHAN Ai-dang. Decomposition kinetics of carbon-doped FeCoCrNiMn high-entropy alloy at intermediate temperature [J]. Transactions of Nonferrous Metals Society of China, 2020, 30(7): 1884−1894.

[26] STEPANOV N D, SHAYSULTANOV D G, CHERNI-CHENKO R S, YURCHENKO N Y, ZHEREBTSOV S V, TIKHONOVSKY M A, SALISHCHEV G A. Effect of thermomechanical processing on microstructure and mechanical properties of the carbon-containing CoCrFeNiMn high entropy alloy [J]. Journal of Alloys and Compounds, 2017, 693: 394−405.

[27] HE L, JIN Z H, LU J D, TANG J. Modulated structures of Fe−10Mn−2Cr−1.5C alloy [J]. Materials & Design, 2002, 23(8): 717−720.

[28] LI Zhi-ming. Interstitial equiatomic CoCrFeMnNi high-entropy alloys: Carbon content, microstructure, and compositional homogeneity effects on deformation behavior [J]. Acta Materialia, 2019, 164: 400−412.

[29] DOHERTY R D, HUGHES D A, HUMPHREYS F J, JONAS J J, JENSEN D J, KASSNER M E, KING W E, MCNELLEY T R, MCQUEEN H J, ROLLETT A D. Current issues in recrystallization: A review [J]. Materials Science and Engineering A, 1997, 238: 219−274.

[30] KANEKO K J, FUKUNAGA T, YAMADA K, NAKADA N, KIKUCHI M, SAGHI Z, BARNARD J S., MIDGLEY P A. Formation of $M_{23}C_6$-type precipitates and chromium-depleted zones in austenite stainless steel [J]. Scripta Materialia, 2011, 65(6): 509−512.

[31] ZHENG Lei-gang, HU Xiao-qiang, KANG Xiu-hong, LI Dian-zhong. Precipitation of $M_{23}C_6$ and its effect on tensile properties of 0.3C−20Cr−11Mn−1Mo−0.35N steel [J]. Materials & Design, 2015, 78: 42−50.

[32] XU Yuan-tao, ZHANG Xi-ying, TIAN Yu-bo, CHEN Chu, NAN Yu-jing, HE Huan, WANG Ming-jia. Study on the nucleation and growth of $M_{23}C_6$ carbides in a 10% Cr martensite ferritic steel after long-term aging [J]. Materials Characterization, 2016, 111: 122−127.

[33] WU Hao, FAN Guo-hua. An overview of tailoring strain delocalization for strength-ductility synergy [J]. Progress in Materials Science, 2020, 113: 100675.

[34] ZHU Yun-tian, AMEYAMA K, ANDERSON P M, BEYERLEIN I J, GAO Hua-jian, KIM H S, LAVERNIA E, MATHAUDHU S, MUGHRABI H, RITCHIE R O, TSUJI N, ZHANG Xiang-yi, WU Xiao-lei. Heterostructured materials: Superior properties from hetero-zone interaction [J]. Materials Research Letters, 2021, 9(1): 1−31.

[35] COOMAN D, BRUNO C, ESTRIN Y, KIM S K. Twinning-induced plasticity (TWIP) steels [J]. Acta Materialia, 2018, 142: 283−362.

[36] WANG Z W, WANG Y B, LIAO X Z, ZHAO Y H, LAVERNIA E J, ZHU Y T, HORITA Z, LANGDON T G. Influence of stacking fault energy on deformation mechanism and dislocation storage capacity in ultrafine-grained materials [J]. Scripta Materialia, 2009, 60(1): 52−55.

[37] SCHRAMM R E, REED R P. Stacking fault energies of seven commercial austenitic stainless steels [J]. Metallurgical Transactions A, 1975, 6(7): 1345−1351.

[38] SAEED A, IMLAU J, PRAHL U, BLECK W. Derivation and variation in composition-dependent stacking fault energy maps based on subregular solution model in high-manganese steels [J]. Metallurgical and Materials Transactions A, 2009, 40(13): 3076−3090.

[39] ABBASI A, DICK A, HICKEL T, NEUGEBAUER J. First-principles investigation of the effect of carbon on the stacking fault energy of Fe−C alloys [J]. Acta Materialia, 2011, 59(8): 3041−3048.

[40] YANG H K, ZHANG Z J, ZHANG Z F. Comparison of work hardening and deformation twinning evolution in Fe−22Mn−0.6C−(1.5Al) twinning-induced plasticity steels [J]. Scripta Materialia, 2013, 68(12): 992−995.

[41] LIU T K, WU Z, STOICA A D, XIE Q, WU W, GAO Y F, BEI H, AN K. Twinning-mediated work hardening and texture evolution in CrCoFeMnNi high entropy alloys at cryogenic temperature [J]. Materials & Design, 2017, 131: 419−427.

[42] WU Z, PARISH C M, BEI H. Nano-twin mediated plasticity in carbon-containing FeNiCoCrMn high entropy alloys [J]. Journal of Alloys and Compounds, 2015, 647: 815−822.
[43] LI J B, GAO B, WANG Y T, CHEN X H, XIN Y C, TANG S, LIU B, LIU Y, SONG M. Microstructures and mechanical properties of nano carbides reinforced CoCrFeMnNi high entropy alloys [J]. Journal of Alloys and Compounds, 2019, 792: 170−179.
[44] KLIMOVA M, SHAYSULTANOV D, SEMENYUK A, ZHEREBTSOV S, STEPANOV N. Effect of carbon on recrystallised microstructures and properties of CoCrFeMnNi-type high-entropy alloys [J]. Journal of Alloys and Compounds, 2021, 851: 156839.
[45] PENG Jian, LI Zi-yong, FU Li-ming, JI Xin-bo, PANG Zhuo-rui, SHAN Ai-dang. Carbide precipitation strengthening in fine-grained carbon-doped FeCoCrNiMn high entropy alloy [J]. Journal of Alloys and Compounds, 2019, 803: 491−498.
[46] WU Xiao-lei, ZHU Yun-tian. Heterogeneous materials: a new class of materials with unprecedented mechanical properties [J]. Materials Research Letters, 2017, 5(8): 527−532.
[47] GAO H J, HUANG Y G. Geometrically necessary dislocation and size-dependent plasticity [J]. Scripta Materialia, 2003, 48(2): 113−118.
[48] ASHBY M F. The deformation of plastically non-homogeneous materials [J]. Philosophical Magazine, 1970, 21: 399−424.
[49] GLADMAN T. Precipitation hardening in metals [J]. Materials Science and Technology, 1999, 15(1): 30−36.
[50] ZHU C, LU Z P, NIEH T G. Incipient plasticity and dislocation nucleation of FeCoCrNiMn high-entropy alloy [J]. Acta Materialia, 2013, 61(8): 2993−3001.
[51] WANG Zhang-wei, BAKER I, CAI Zhong-hou, CHEN Si, POPLAWSKY J D, GUO Wei. The effect of interstitial carbon on the mechanical properties and dislocation substructure evolution in $Fe_{40.4}Ni_{11.3}Mn_{34.8}Al_{7.5}Cr_6$ high entropy alloys [J]. Acta Materialia, 2016, 120: 228−239.

含碳 FeCoCrNiMn 高熵合金的异质显微组织和力学性能

郭 林[1,2]，顾 及[2]，戴翌龙[1]，林建国[1]，宋 旼[2]

1. 湘潭大学 材料科学与工程学院，湘潭 411105；
2. 中南大学 粉末冶金国家重点实验室，长沙 410083

摘 要：利用可控热机械处理工艺，在含 0.5%C(摩尔分数)的 FeCoCrNiMn 高熵合金中获得具有纳米析出相和双峰晶粒尺寸分布的异质显微组织。粗大的 $M_{23}C_6$ 碳化物倾向于在细晶粒的晶界处形成。与具有均匀显微组织的样品相比，异质结构 FeCoCrNiMn−0.5%C(摩尔分数)高熵合金具有相似的平均晶粒尺寸(约 4.8 μm)。然而，它具有晶粒双峰结构且粒径<3 μm 的细晶粒的体积分数更高，从而使屈服强度从 552 MPa 提高到 632 MPa。具有异质结构的样品在不同的区域呈现不同的力学性能和变形显微组织，导致在拉伸变形过程中产生明显的应变局域化和高密度的几何必要位错。这些变形特征有利于提高应变硬化能力，从而促进强度−塑性的协同作用。

关键词：高熵合金；异质显微组织；双峰晶粒；力学性能；强化机制

(Edited by Wei-ping CHEN)